

Use Authorization

In presenting this thesis in partial fulfillment of the requirements for an advanced degree at Idaho State University, I agree that the Library shall make it freely available for inspection. I further state that permission to download and/or print my thesis for scholarly purposes may be granted by the Dean of the Graduate School, Dean of my academic division, or by the University Librarian. It is understood that any copying or publication of this thesis for financial gain shall not be allowed without my written permission.

Signature _____

Benjamin Nield

Date _____

Calibration Method for B-dot Magnetic Field
Probes for Use in Pulsed Power Experiments

Benjamin Nield

A thesis

submitted in partial fulfillment

of the requirements for the degree of

Master of Science

Nuclear Science and Engineering

at

Idaho State University

Fall2014

To the Graduate Faculty:

The members of the committee appointed to examine the thesis of BENJAMIN NIELD find it satisfactory and recommend that it be accepted.

George Imel,

Major Advisor

Mahbub Khandaker,

Graduate Faculty Representative

Chad Pope,

Committee Member

Contents

List of Figures	vi
List of Tables	vii
Abstract	viii
1 Introduction	1
1.1 Pulsed-Power	1
1.1.1 Pulsed-power and Pinches	5
2 Electromagnetic Theory of Pulsed-Power	6
3 Calibration	12
3.1 Calibration Theory.....	14
3.2 Circuit Simulation.....	15
3.3 Electromagnetic Modeling.....	17
3.3.1 XF7 Solver.....	17
3.3.2 Model.....	18
3.4 Calibration System	26
3.5 Current-Viewing Resistor	28
3.6 Calibration Method.....	29

4	Results	33
5	Discussion and Analysis	37
5.1	Variance of the Runs	37
5.2	Scaling Factor	40
5.3	Polynomial Fit.....	40
5.4	Peak Matching	44
6	Error Analysis	47
7	Future Work	49
7.1	Error Reduction	49
7.2	Interfacing With Other Probes	50
8	Conclusion	51
	References	52

List of Figures

1	RLC Circuit Damping	9
2	Circuit Model	15
3	Expected Voltage vs. Time	16
4	Simulated Current Density	20
5	Current Density Comparison Between Two Models	21
6	Simulated B-field for Shorter Model	22
7	Simulated B-field for Longer Model	23
8	Simulated Current	25
9	CVR Diagram.....	29
10	Power Dissipated in CVR.....	30
11	Experimental Setup Diagram.....	30
12	A photograph of the completed setup.....	31
13	Results at 1 kV	33
14	Results at 1.25 kV	34
15	Results at 1.5 kV	35
16	Results at 2 kV	36
17	Polynomial Fits.....	41
18	Ratio of the two Polynomials.....	45

List of Tables

1	Difference from the mean, V_{run}/V_{avg} , for each of the five CVR outputs at each voltage.	38
2	Difference from the mean, V_{run}/V_{avg} , for each of the five B-dot outputs at each voltage.	39
3	The average residuals between the fit curve and the data.	42
4	The R^2 goodness of fit values for the 5-th order polynomial curve fit to the unbinned data.	43
5	The R^2 goodness of fit values for the 5-th order polynomial curve fit to the binned data. Each bin contained 100 points (40 ns). . .	43
6	Average Ratio Between the Two Curves.....	46
7	The factors by which the B-dot signal needed to be multiplied to calibrate with the CVR.....	47

Abstract

Characterization and measurement of magnetic fields is important to pulsed-power plasma experiments. Fast and compact magnetic field probes have been developed to measure rapidly changing magnetic fields. We developed a method for calibrating the probes at higher current and lower uncertainty than existing methods. We show a simple setup for calibration of a loop-type magnetic field probe and a method of calibration with a tolerance of 5% with potential to achieve even better tolerance in the future. The results are compared to those suggested by electromagnetic theory. We find that this setup should allow for more accurate determination of magnetic fields in pulsed-power experiments than existing methods.

1 Introduction

Pulsed-power accelerators are used for a variety of high energy-density physics experiments, such as radiation physics, inertial confinement fusion and astrophysics. Such experiments use rapidly changing high-energy plasmas, which can be difficult to characterize. Knowledge of the magnetic field behavior is often crucial to understanding the behavior of the plasma [1].

1.1 Pulsed-Power

Pulsed-power, originally called 'pulse-power' is the technique of storing electrical energy (e.g., in a capacitor bank) and releasing it in a very short pulse. The amount of power is a function of both the energy stored and the time over which it is released. The equation relating the two is:

$$P = \frac{E}{t} \quad (1)$$

Where P is the power, E is the energy stored, and t is the time over which it is released. The shorter the time period over which the pulse takes place, the greater the power for a given E [2].

The energy is initially stored in capacitor banks and discharged rapidly into pulse-forming lines. These lines act as voltage multipliers, further accelerating the charges. The energy is then transferred to transmission lines which must be heavily insulated to avoid electrical field breakdown at the high voltages. The

transmission lines connect to a cathode and anode in order to produce an electron beam. In the early pulse-power experiments, x-ray tubes were used whereas more modern setups use a diode [2].

In the 1950s and 1960s, it was realized that radiation from nuclear explosions (neutrons, x-rays and gamma rays) would produce electromagnetic pulses which could damage electronics. Testing and hardening electrical components against electromagnetic pulses became an active area of research [2]. Pulsed-power technology was used to simulate the electromagnetic pulses from a nuclear weapon. The high-energy electron beam generated by a pulsed-power setup was targeted at a metal. The collision of the electrons with the metal produces gamma-rays in a process known as bremsstrahlung [2].

Bremsstrahlung means 'braking radiation' in German. It is the radiative energy released by the deceleration of charged particles. Electrons, because of their low mass, produce more bremsstrahlung radiation than protons or other charged particles. The moving particle loses kinetic energy as it slows down and this kinetic energy is released as photons. The greater the change in kinetic energy, the higher the frequency of the produced photon. Thus, it is of importance that the electrons in pulsed-power experiments are accelerated to high velocities in order to produce the higher frequency gamma and x-rays [3].

As a charged particle passes the target, it experiences the effect of the target's

electro-magnetic field at the surface. The field of the target accelerates (deflects) the charged particle with an impulse lasting a time $\tau = b/v_0$ where b is the impact parameter and v_0 is the velocity of the incoming particle. As the charge experiences this impulse, it radiates power given by the relation [4]

$$P^t = \frac{q^2 \dot{v}^2}{4\pi E_0 3c^3} \quad (2)$$

where P^t is the radiated power, q is the charge, \dot{v} is the acceleration of the charged particle, E_0 is the permittivity of free space, and c is the speed of light in a vacuum. Integrating this relation over time yields the total radiated energy [4]. The total energy radiated in a single collision can be estimated by taking the characteristic value of the acceleration to be that given by the electric field force at the closest approach of the particle,

$$\dot{v} = q\mathbf{E}/m_1 = \frac{q_1 q_2}{4\pi E_0 b^2 m_1} \quad (3)$$

and using that to derive an estimate of the radiated power [4]

$$P^t = \frac{q_1^4 q_2^2}{(4\pi E_0)^3 3c^3 m_1^2 v_0 b^3} \quad (4)$$

To obtain the energy, W , lost per unit length we integrate over the impact parameters and multiply by the density of the target, n_2

$$\frac{dW}{dl} = n_2 \int_{b_{min}}^{b_{max}} \frac{q_1^4 q_2^2}{(4\pi E_0)^3 3c^3 m_1^2 v_0 b^3} 2\pi b db = n_2 \frac{q_1^4 q_2^2}{(4\pi E_0)^3 3c^3 m_1^2 v_0} \frac{4\pi}{b} \Big|_{b_{min}}^{b_{max}} \quad (5)$$

We can assume the upper limit to be infinity because of the $1/b$ behavior of the integral. The lower limit is taken to be the quantum limit at which the wave nature of the particle becomes important [4],

$$b_{min} = \frac{\hbar}{m_1 v} \quad (6)$$

The energy radiated per unit length then becomes [4]

$$\frac{dW}{dl} = n_2 \frac{q^4 q^2}{(4\pi E_0)^3} \frac{4\pi}{3c^3} \frac{1}{m_1 \hbar} \quad (7)$$

For collisions where the electron collides with a nucleus, the above equation can be written as [4]

$$\frac{dW}{dl} = n_2 Z^2 m_e c^2 a \frac{4\pi}{3} r_e^2 \quad (8)$$

where a is the fine structure constant, $e^2/4\pi E_0 \hbar c$, and r_e is the classical electron radius, $e^2/4\pi E_0 m_e c^2$ [4].

Producing high-energy radiation such as x-rays and gamma-rays requires high power. In order to run the tests with high power but without using large amounts of energy, a very short pulse is needed. Pulsed-power setups are therefore better suited to applications requiring x-ray or gamma-ray production, because they can produce the requisite high powers and currents at a lower total energy.

1.1.1 Pulsed-power and Pinches

An x-pinch is when a massive amount of current is put through a thin wire, vaporizing it. The magnetic forces produced compress the resulting plasma further. Pinches are of interest to the study of magnetic confinement fusion, but can also provide a particle heating and compression mechanism for inertial confinement fusion. For example, the wire, when vaporized, becomes a conducting plasma and carries a very high current. The current creates a magnetic field encircling the plasma and the force of that field on the conducting plasma squeezes it inwards, through $J \times B$ action, imploding it. The implosion releases x-rays which then could be used to compress a deuterium-tritium fuel capsule and confine it sufficiently so that it fuses, releasing energy. Progress in pulsed-power technology has led to interest in using pinches for inertial confinement fusion [2][3].

2 Electromagnetic Theory of Pulsed-Power

In order to accelerate the electrons in a pulsed-power system, a force must be applied to them. Pulsed-power systems accelerate charges electrostatically through the application of electric field. A charged particle is subjected to a force due to an electric field as described by the following equation:

$$\mathbf{F} = q\mathbf{E} = -q\nabla\varphi = m\frac{\partial\mathbf{v}}{\partial t} \quad (9)$$

The kinetic energy of the particle can then be given

$$K = \int \mathbf{F} \cdot d\mathbf{x} \quad (10)$$

$$m\frac{\partial\mathbf{v}}{\partial t} \cdot \frac{\partial\mathbf{x}}{\partial t} = -q\frac{\partial\varphi}{\partial x} \quad (11)$$

$$m\mathbf{v} dv = -q d\varphi \quad (12)$$

$$\frac{1}{2}m(\mathbf{v}^2 - v_0^2) = -q(\varphi - \varphi_0) \quad (13)$$

where m is the mass of the electron, \mathbf{v} is its velocity, t is the time, q is the electron charge, x is the spatial coordinate, and φ is the scalar potential [5]. Thus, we see that applying a voltage to a charged particle will accelerate the particle and increase its kinetic energy as it moves through the potential.

The voltage can be applied through a direct current source such as a high-voltage transformer with diodes or a Van de Graaff generator, or in the case of pulsed-power, by a pulsed voltage.

Pulsing the voltage has several benefits over direct current voltage that pulsed-power experiments capitalize on. When dealing with very high-voltages, breakdown of the dielectric is a concern. However, sufficiently fast pulses can apply the potential to a particle in less time than it takes for breakdown or other detrimental effects to occur [5].

Fast pulses are also useful for viewing fast phenomena. Generating a fast x-ray pulse can be used to observe events which take place over very short timescales [5].

For experiments which involve very high power, releasing the energy in fast pulses increases the power without increasing the total energy used (see Equation 1).

Pulsed-power systems can be described in an ideal case by a capacitor, inductor and resistor connected in series. A switch connects the pulsed-power system to the resistive load.

The switch is initially open as the capacitor charges. To fire the pulse, the switch is closed and the capacitor rapidly discharges through the resistive load.

The governing differential equation for this process is:

$$L \frac{d^2 i}{dt^2} + (R + R_L) \frac{di}{dt} + \frac{1}{C} i(t) = 0 \quad (14)$$

where L is the inductance, i is the current, R is the resistance of the resistor, R_L is the resistance of the load, and C is the capacitance [5].

For initial conditions we have

$$\begin{aligned} i(t=0) &= 0 \\ \frac{di}{dt}(t=0) &= \frac{V_0}{L} \end{aligned} \quad (15)$$

where V_0 is the initial voltage to which the capacitor is charged.

From these conditions, it is convenient to define the frequencies $\omega_0 = 1/\sqrt{LC}$, $\omega_1 = \sqrt{\omega_0^2 - \beta^2}$, and $\omega_2 = \sqrt{\beta^2 - \omega_0^2}$, where $\beta = (R + R_L)/2L$. Note that ω_1 and ω_2 have units of inverse time.

We also have the phase shift $\delta = \tan^{-1} \beta/\omega_1$.

This leads naturally to three classes of solutions for the original differential equation. The first case is known as 'underdamped' and occurs when $\omega_0 > \beta$

$$i(t) = \frac{CV_0}{\cos\delta} \exp(-\beta t) [\omega_1 \sin(\omega_1 t - \delta) + \beta \cos(\omega_1 t - \delta)] \quad (16)$$

The second case is called 'overdamped' and occurs when $\omega_0 < \beta$

$$i(t) = \frac{CV_0(\beta^2 - \omega_0^2)}{2\omega_2} [\exp(\omega_2 t) - \exp(-\omega_2 t)] \exp(-\beta t) \quad (17)$$

The third case is the 'critically damped' case where $\omega_0 = \beta$

$$i(t) = \beta CV_0 (\beta t) \exp(-\beta t) \quad (18)$$

These three cases are shown graphically in Figure 1.

Maximum energy transfer occurs in the critically damped case. The impedance of the circuit in the critically damped case will be $R = R_c = 2\sqrt{L/C}$ since $\omega_0 = \beta$ [5].

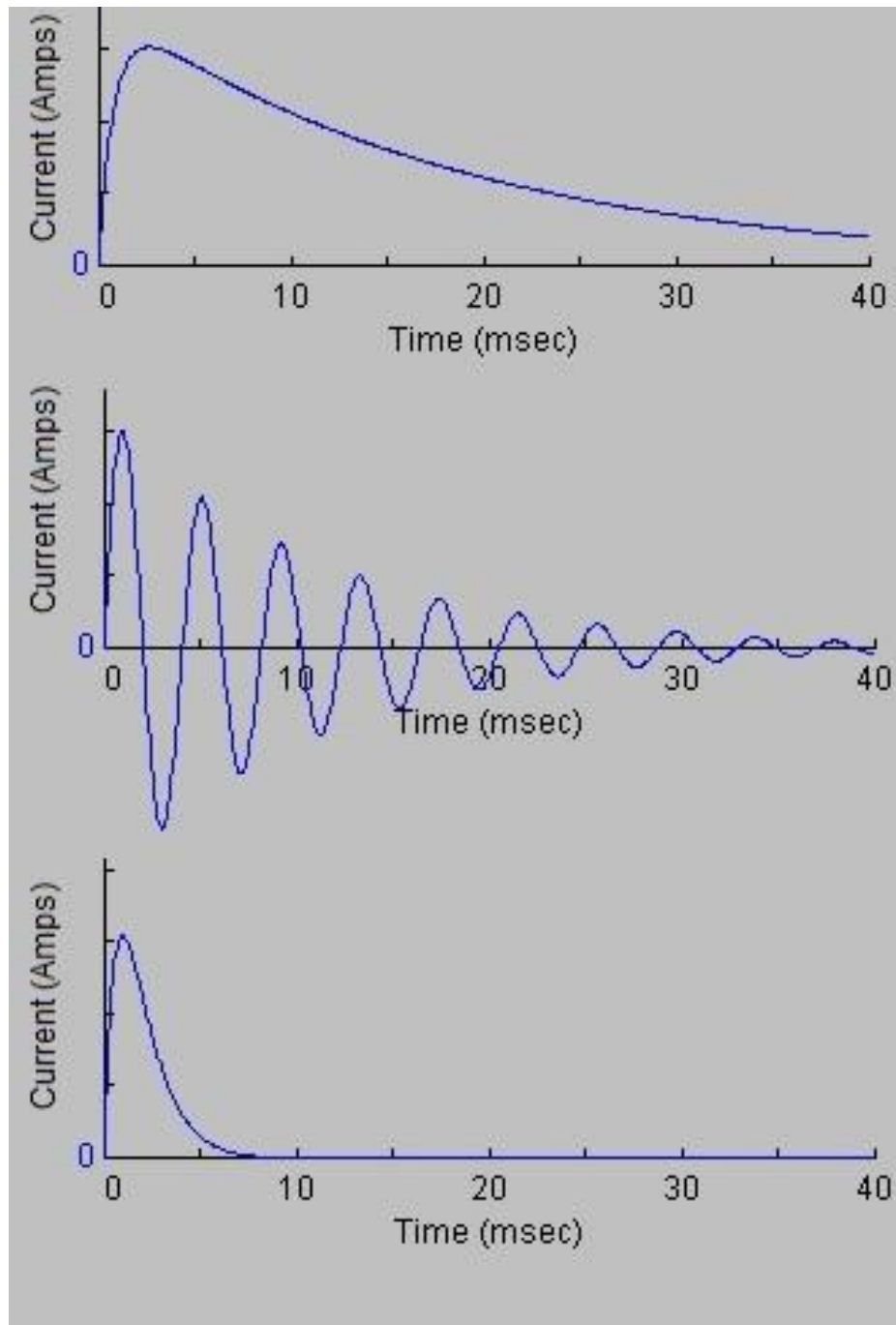


Figure 1: The three cases of damping for RLC circuits. Overdamped (top), underdamped (middle), and critically damped (bottom) [6].

In order to create a pulse, it is necessary to charge a capacitor to some voltage. The pulse length may be set by changing the inductance of the circuit.

For this pulsed-power experiment, we use a pulse forming line setup, which is characterized by two inductors separated by an insulator. To form the pulse, the transmission line is charged using pulsed high voltage. The resistive load between the two plates is attached at the end of the transmission line. The pulse is then discharged into the load.

The characteristic impedance is given by the properties of the material used in the strip-line conductors [5].

$$Z_0 = \sqrt{\frac{\mu}{\epsilon}} \quad (19)$$

where μ is the permeability of the material and ϵ is the permittivity.

A pulse on the strip-line moves at phase velocity [5]

$$v_p = \frac{1}{\sqrt{\mu/\epsilon}} \quad (20)$$

At the end of the line we expect some of the pulse to be reflected because of the changing impedance at the interface. The reflection coefficient is given by

$$\Gamma = \frac{Z_2 - Z_1}{Z_2 + Z_1} \quad (21)$$

with Z_1 and Z_2 being the impedance of the two materials, which gives the reflected voltage $V_{refl} = \Gamma V_i$ and the reflected power $P_{refl} = \Gamma^2 P_i$ in terms of the initial voltage, V_i , and initial power, P_i [5].

Magnetic field and conductivity and magnetic flux are all important properties and concepts for a theoretical modeling of this work. Maxwell's equations form the foundation of classical electrodynamics by showing the relations between the magnetic and electrical field. Maxwell's equations are given in vector form:

$$\nabla \times \mathbf{H} = \mathbf{j} + \frac{\partial \mathbf{D}}{\partial t} \quad (22)$$

$$\nabla \times \mathbf{E} = -\frac{\partial \mathbf{B}}{\partial t} \quad (23)$$

$$\nabla \cdot \mathbf{B} = 0 \quad (24)$$

$$\nabla \cdot \mathbf{D} = \rho \quad (25)$$

where \mathbf{H} is the magnetic field strength, \mathbf{B} is the magnetic flux density, \mathbf{D} is the electric flux density, \mathbf{E} is the electrical field strength, and \mathbf{j} is the current density. ρ is a scalar representing the density of free electric charges. We also have the material properties of magnetic permeability, μ , and dielectric permittivity, ϵ , which relate the electric and magnetic flux densities to the electric and magnetic field respectively [7].

$$\mathbf{B} = \mu \mathbf{H} \quad (26)$$

$$\mathbf{D} = \epsilon \mathbf{E} \quad (27)$$

3 Calibration

There are numerous existing ways to calibrate the signal of the magnetic field probe. One of the most common is to generate a magnetic field of known strength and compare the resulting signal of the probe to the known strength of the field. The magnetic field may be generated in a number of ways whether by a Helmholtz coil, a loop, or a straight wire. The various ways of generating field each come with their own drawbacks [8] [9].

A Helmholtz coil may be used to compare its output to the output of the B-dot probe to be calibrated. Helmholtz coils generate uniform field at their center given by the equation

$$B_z = \frac{\mu_0 N I}{a} \frac{8}{5^{3/2}} \quad (28)$$

where a is the coil radius, N is the number of turns in the coil, and I is the current in the coils [9]. Helmholtz coils are generally the preferred method for calibration of B-dot probes, but in order to be accurate it is necessary to know precisely the current, I , in the coils as well as have accurate measurements of the coil radius. The frequency response of the coil must also be considered, based on its capacitance and inductance [9].

Using a straight wire to generate the magnetic field will provide a simple well-defined field at high-frequencies but faces the challenge of the high-current needed to generate a field. Additionally, the uniformity of the field suffers and the high

gradient may make calibration difficult [9].

A main issue for current calibration is the lack of precise knowledge of the geometry of the magnetic field and magnetic field diff in solid conductors. It has been proposed to build calibrated current monitors by computationally modelling the magnetic field diff with a 3-D EM code. This could be a path toward better understanding of the physics involved, but is not a very good calibration idea. The use of different materials and the geometries involved makes obtaining an accurate calibration difficult. For example, copper is used in the bodies of magnetic field probes and in electrodes in order to minimize current diff and in order to simulate this, exact details about the copper need to be known. Simulation of the actual diff to better than a one percent accuracy depends on knowledge of the exact alloy of copper, the time history of the current pulse, the magnitude of the current, the current contacts, the exact as built mechanical details of the monitor, and the mechanical shape of the conductor [10]. Simulating each of these details to the required accuracy would be computationally prohibitive.

Current practice for calibrating magnetic field probes is to create a test current pulse of exactly the same pulse shape as the experimental one and use a calibration geometry exactly the same as the experimental geometry. Each magnetic probe would be calibrated for use only in that calibration field. However, diff of up to ten percent between monitors have been observed due to manufacturing

tolerances [10].

For the reference in this work we use a current viewing resistor (CVR). A CVR was chosen because it has the necessary fast time response needed for pulsed-power calibration as well as the resilience to withstand the high currents to be discharged through it. The particular CVR used in this work is described in Section 3.5.

3.1 Calibration Theory

The governing physics of B-dot probes is Faraday's law

$$E = -N \frac{\Delta\Phi}{\Delta t} \quad (29)$$

Where E is the induced electromotive force (EMF), N is the number of turns of the coil, and $\Delta\Phi/\Delta t$ is the change in magnetic flux per time.

Since the area of the loop is constant, the change in flux will give the time rate of change of the magnetic field $\Delta B/\Delta t$, which is also written as \dot{B} from which notation B-dot probes take their name [11].

The expected voltage signal of capacitor discharge is an exponentially decaying cosine function.

$$e^{-t/\tau} \cos(\omega_1 t + \varphi) \quad (30)$$

where τ is the time constant of decay, t is time, ω_1 is the frequency and φ is the phase.

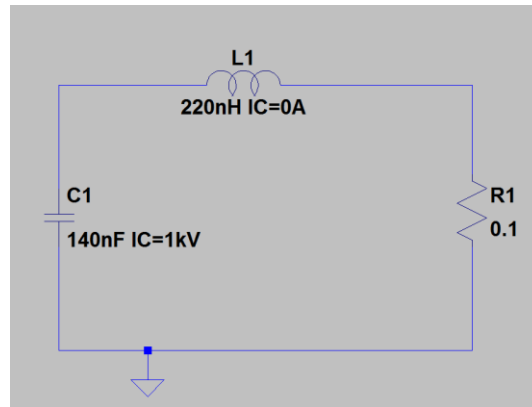


Figure 2: The circuit model of the setup produced with LTSpice IV for simulating the current produced in the CVR when the capacitors are charged to 1 kV.

This equation is given by an electrophysical consideration of RLC circuits. The frequency of such circuits, ω_1 is given by $1/\sqrt{LC}$ and the time constant by $\tau = R/2L$.

3.2 Circuit Simulation

The voltage output of the CVR was simulated using a circuit analysis program LT Spice IV [12]. The calibration system was modeled as an RLC circuit shown in Figure 2.

The voltage predicted by the simulation is shown in Figure 3

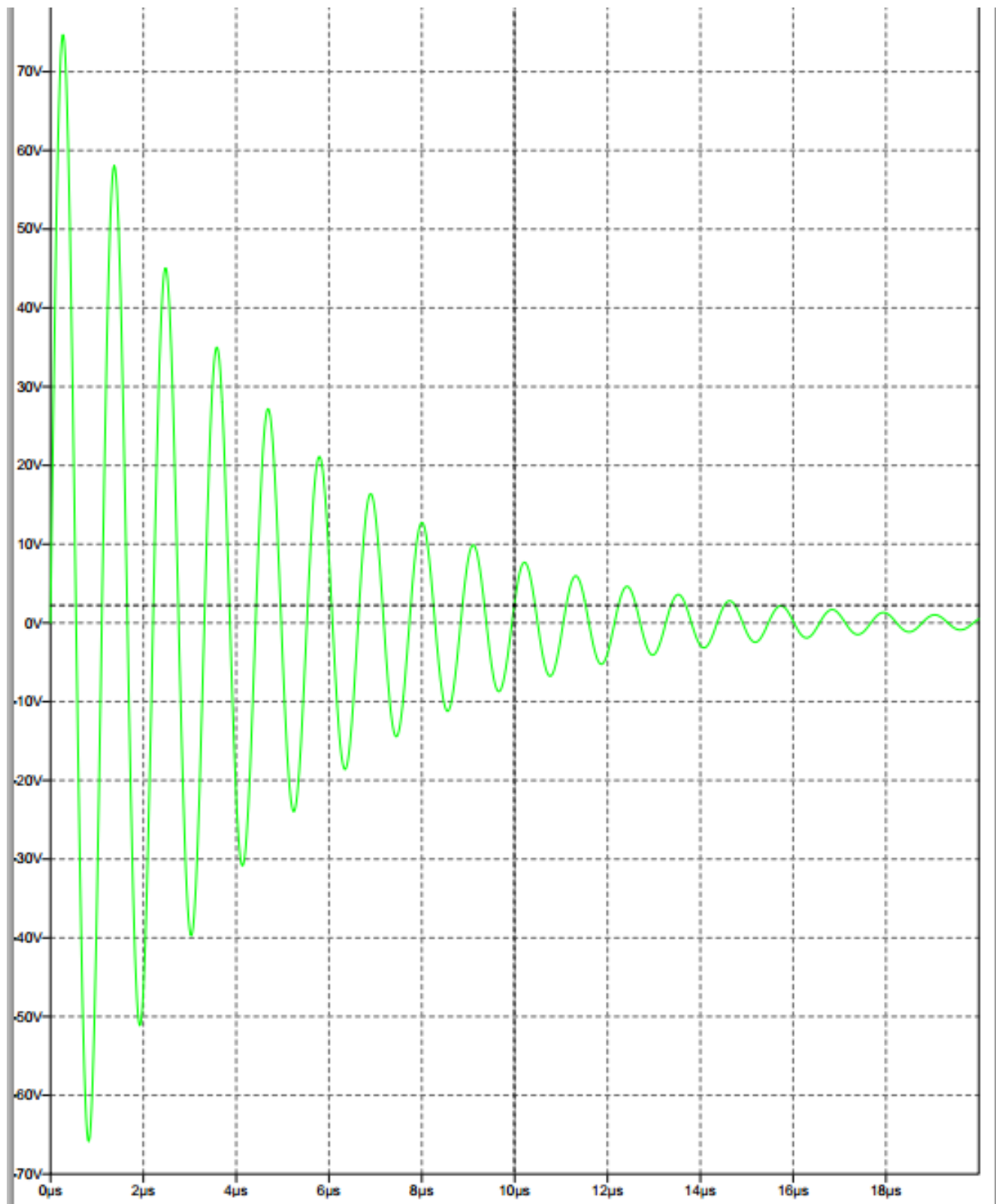


Figure 3: Simulated output from the CVR when the capacitors were charged to 1 kV. Volts are on the vertical axis and time on the horizontal axis.

3.3 Electromagnetic Modeling

To demonstrate the theoretical concepts discussed in the preceding sections on electromagnetic theory as it pertains to the calibration experiment, we employed finite element modeling software. This software was able to provide graphical outputs of the current density and allowed us to select an appropriate geometry for our waveguide strip-line.

3.3.1 XF7 Solver

The modeling software used for this project was Remcom's XF7-FDTD solver [13]. It is a 3-D electromagnetic simulation software which solves Maxwell's equations in both the frequency-domain and the time-domain. This capability allowed a view of the changes in the electromagnetic fields at each point in time. In a frequency-domain-time-domain (FDTD) model, space is segmented into cubic cells. Electric fields are located on the edges of each cell and magnetic fields on the faces. When these cells are small compared to the wavelength, accurate simulations can be performed and continuity can be achieved in the limit of infinite cell size. Time is also discretized, and the step-size is the time it takes for the field to travel from one cell to an adjacent one [14]. The cells are combined together to form the three-dimensional model. This collection of cells is called the mesh. Each cell has three electric fields and three magnetic fields associated with it even though they

share edges and faces with neighboring cells. Materials can be defined by specifying how the fields are calculated at given locations. For instance, a conductor would be represented by a cell edge with an electric field of zero. Joining a series of these cells together would produce a perfectly conducting wire. Similar principles may be used to build various three-dimensional geometries. The cell size is specified by the user. Smaller cells give more resolution but take more computational power. The maximum cell size is usually set such that ten cells can make up a wavelength of the excitation wave. So, for an 8 GHz frequency wave moving at the speed of light, the maximum cell size would be,

$$\frac{c}{8\text{GHz} \times 10} = 3.75 \text{ mm} \quad (31)$$

Excitations are applied to the cells at the start of the simulation using a user-defined waveform. The value of this waveform is added to the field of certain cells and then allowed to propagate until a certain user specified criterion of convergence is met or until a user-defined time limit is reached [14]. For this study, the simulation was allowed to run for a preset time which allowed the characteristic shape of the waveform to appear.

3.3.2 Model

The model simulated in XF7 [13] consisted of two strip-line plates made of ideal conductors separated by a 10 mil thick sheet of mylar for which the appropriate

electrical properties were specified. The plates were joined by an ideal resistor of 0.1 Ohms with a series inductance of 200 nH to represent the inductance of the circuit.

A long strip-line with width approximately 1/5 the length was theorized to provide the uniform current needed to produce a clear signal for the sensors. To demonstrate this, a model of two plates 50 inches long and 5 inches wide was created and compared to a model of two plates which were 5 inches square. The strip-lines were defined to be perfect conductors. Defining the material properties of aluminum, while possible in the software, would add unnecessary complications to the model. Aluminum is a good enough conductor that it can be modeled as a perfect conductor, in order to simplify the code and reduce the runtime of the simulation.

A current source of 1 kA was applied to one of the pair of plates to represent the discharge of a capacitor bank. The current source used a Gaussian waveform with a rise time of 10 nanoseconds to represent a fast pulse discharge from the capacitors.

It was determined that a long, relatively narrow strip-line terminating in a point would yield the most uniform current density, while also minimizing reflections. A visualization of how the strip-line geometry behaves when exposed to a current source is shown in Figure 4.

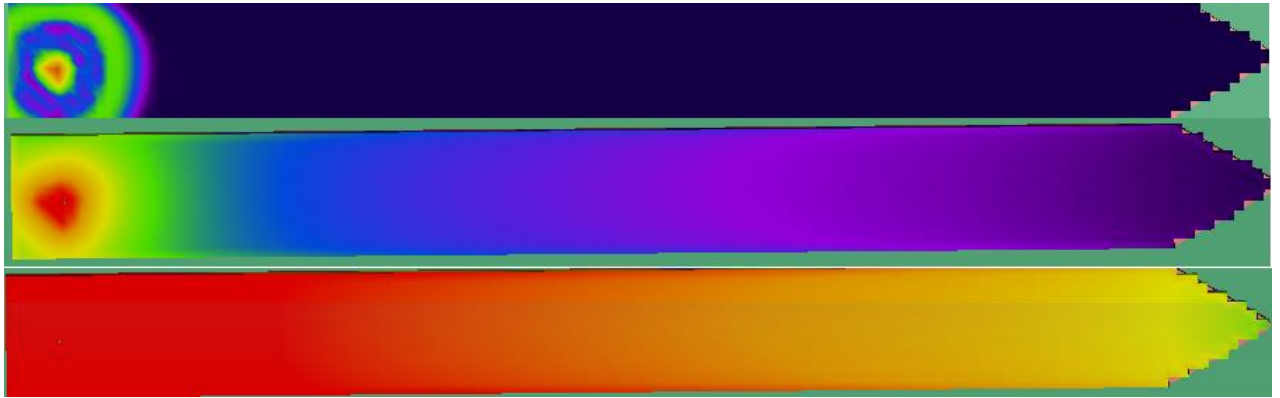


Figure 4: Visualization of the current density over time. The top picture shows just after the discharge (3 ns), the middle shows the current traveling down the stripline (8 ns), and the bottom shows the current becoming uniform over the length of the line (24 ns).

To eliminate field breakdown at the sharp-edges, the edges were rounded down to a quarter-inch radius.

The long strip-line model performed much better than the shorter version in the uniformity of the current produced. Figure 5 compares the shorter model and the longer model to show how the current is able to become more uniform with the longer design. The current density near the middle and right side of the longer model shows a current density that differs by less than an order of magnitude, whereas the current density in the short plate ranges across several orders of magnitude on the right-hand side.

Additionally, the B-field produced by the longer strip-line model is much more

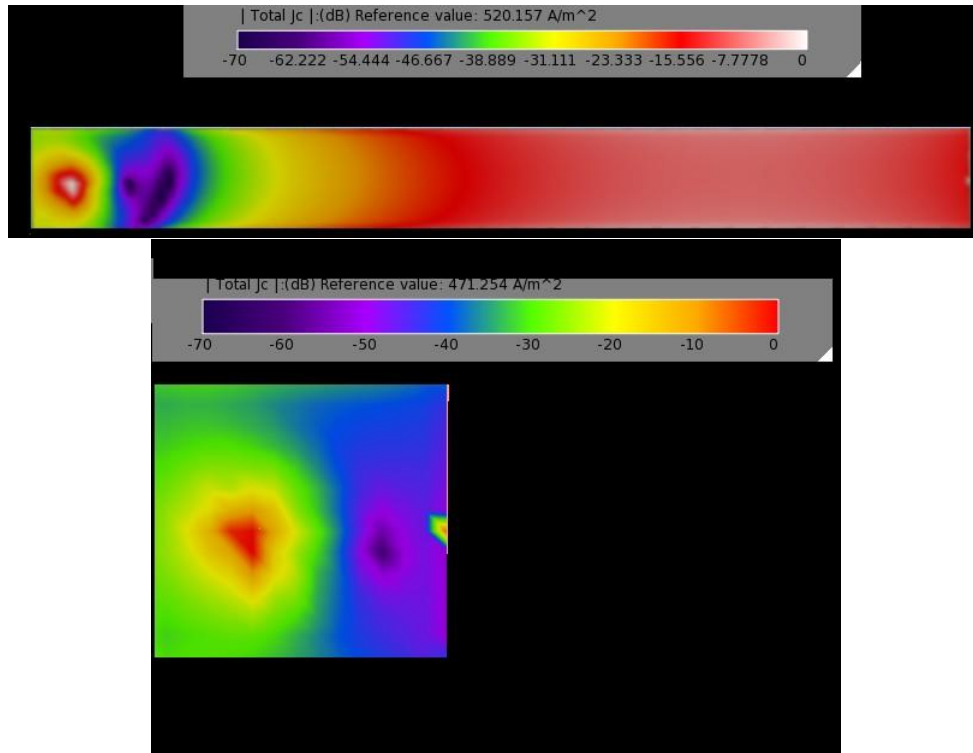


Figure 5: The longer strip-line model (top) allows the current to achieve more uniformity than the shorter model (bottom). Neither of these models have the tapered end used in the final design. These visualizations are from 33 ns after the simulated discharge.

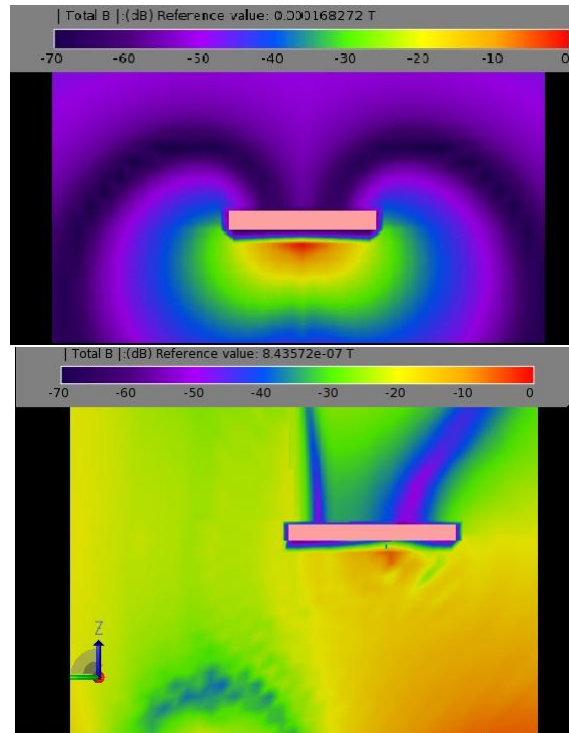


Figure 6: Side-view of the shorter plate model at 3 ns (top) and 33 ns (bottom) after simulated discharge. The B-field produced by the shorter model was not uniform compared with the longer plate model in Figure 7.

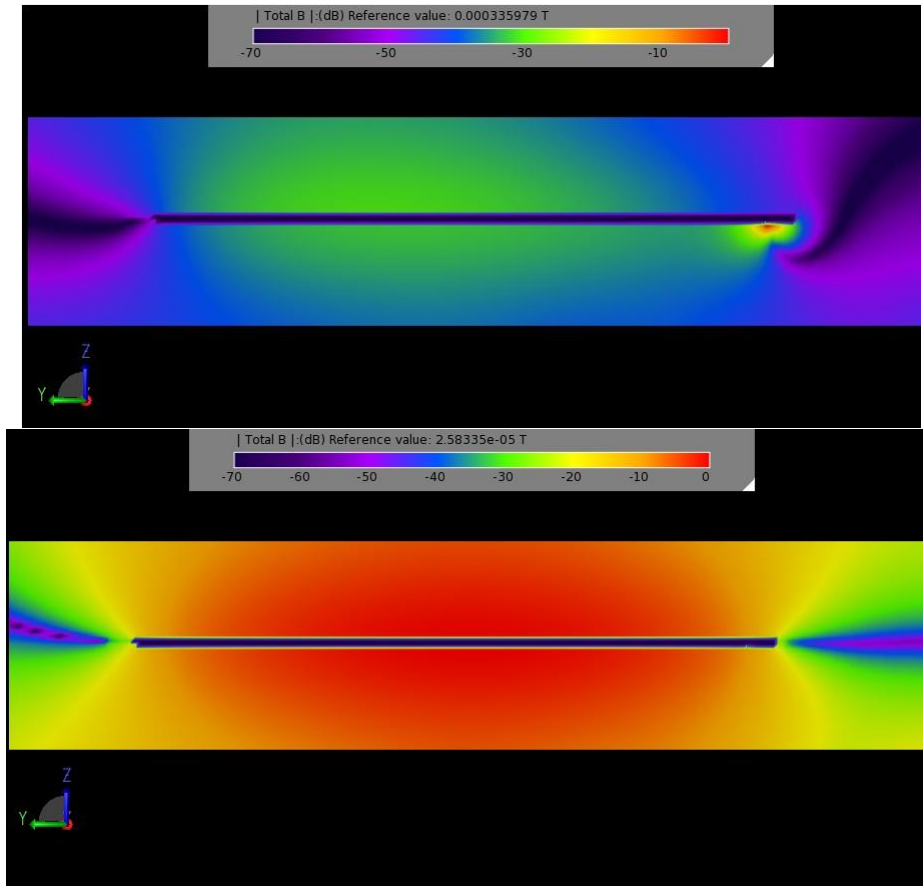


Figure 7: Visualization of the B-field produced by the capacitor discharge for the longer plate model. This is a side view of the model with the point to which the capacitor discharged on the bottom right of the plate. The second picture shows the B-field becoming more uniform as the current has a chance to propagate. The times shown are for 3 ns and 18 ns after simulated discharge

uniform than the one produced by the shorter design. See Figure 6 for the simulation of the B-field for the shorter plates. Figure 7 shows the behavior of the B-field in the longer plate model. The B-field is much more uniform, especially around the region of interest near the middle of the plate. The longer plate model shows B strength difference of less than an order of magnitude in that region, while the shorter plate model shows difference of several orders of magnitude in the B strength in that region. Near the discharge point on both models, the B becomes asymmetric because the current source is applied locally to a single point on one side of the plate. This point discharge causes the local magnetic B to behave in a non-uniform manner. In order to obtain a uniform B and current for the experiment, it is necessary to take measurements further away from this point where the field has become more uniform. A longer plate allows the current to distribute uniformly and the B-field to become more uniform further from the discharge point. If the B were visualized near the discharge point on the longer model, there would be similar non-uniformities in the B as those seen in the shorter plate model. Thus, both the longer-plate model and the idea of mounting the B-dot probe in the center of the plate received validation from the model.

The current through the simulated resistor was also tracked by the software. This enabled a check to see if the more idealized circuit simulation performed in Section 3.2 was accurate. The current output by the model is seen in Figure 8.

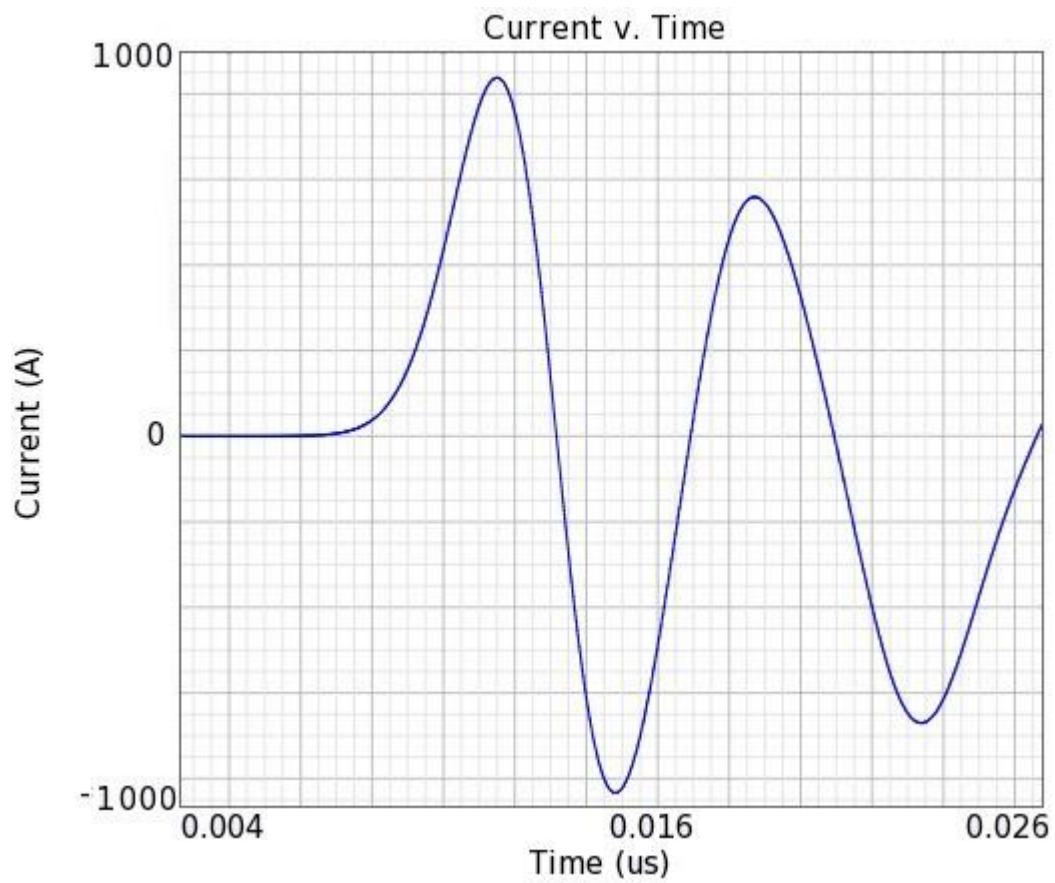


Figure 8: The current through the simulated resistor for a 1 kA discharge.

The shape of the current graph is qualitatively similar to the output of the circuit simulation carried out in LT Spice (Figure 3), and shows an exponentially decaying cosine function which is what was expected given the calculations in Section 3.1.

3.4 Calibration System

To produce the uniform current needed for a reliable signal from the B-dot probe, a simplistic strip-line geometry was used. This setup consisted of two long metal plates insulated from each other by 10-mil mylar sheeting. Aluminum was chosen as the conducting material as it is a cheap and common conductor. The plates were of 0.25 inch thickness to sustain mechanical stability and to have enough thickness to mount the B-dot probe.

The two plates were stacked one on top of the other. Uniform current, being necessary for the reliability of the signal, was achieved by employing strip-lines ten times longer than their width. The plate to which the current was applied, henceforth referred to as the 'hot plate,' was tapered to a point at one end to allow the current to converge and minimize reflection as explained in the previous section. The CVR was mounted at the end of the tapered point. The two plates were both 50 inches long. The hot plate was 5 inches wide and the ground plate

was 10 inches wide. The taper of the hot plate began 5 inches from the end.

A narrow spacing between the plates ensured current uniformity. The spacing between the plates was 10-mil mylar sheeting which was kept fl by four clamps joining the two plates together. To prevent the clamps from conducting, mylar insulation was used at each clamping site.

The energy needed for the pulse was stored in four 35 nano-farad capacitors connected in parallel. They were discharged by means of a metal strip protruding from the bottom capacitor. This strip was pressed down by an insulated rod until it contacted the top aluminum plate, at which point the capacitors discharged in a pulse.

Since pulsed-power experiments use very high current, a more accurate calibration must also take place at a high current [10]. We thus used a 2.5 kV high voltage power supply to generate the high currents needed.

The capacitors were charged by a 5000 Ohm resistor and the 2.5 kV power supply. The power supply was attached to the resistor by high-voltage cabling.

The B-dot probe design used for the calibration was the B2-L2 B-Dot from Sandia National Laboratories (Part No. J10977-000). The L2 type B-dot is a wire loop of approximately 1/8 of an inch outer diameter mounted in a metal casing which was then mounted to the ground plate by two screws. The probe was mounted such that the open face of the loop was perpendicular to the path of the

current to ensure maximum electromagnetic flux through the loop. Perpendicularity was ensured through the use of a square in marking the mounting holes. The signal from the wire loop was output to an oscilloscope.

3.5 Current-Viewing Resistor

The key component of this calibration setup is the current-viewing resistor. To achieve high-precision calibration, the reference value must have a precision equal to or better than the precision that is hoped to be achieved. Current-viewing resistors are ruggedly designed and are able to sustain high peak power generated by capacitor banks or pulse-generator systems.

CVRs have a set energy capacity at which they are rated. This rating is defined as

$$E_{max} = R_{CVR} \int_{max} i^2 dt \quad (32)$$

This is the maximum amount of energy that should be discharged through the capacitor in a time period under which losses are negligible.

The current-viewing resistor selected was a TandM Research SSDN-10 0.010 $\pm 1\%$ Ohm with threaded mounting (Figure 9), which was mounted to the two plates through a 0.25 inch diameter hole and held in place with brass nuts. The hole on the ground plate side was threaded, allowing the CVR to screw in and ensure good connection and common ground. A small 'x' was cut in the insulating

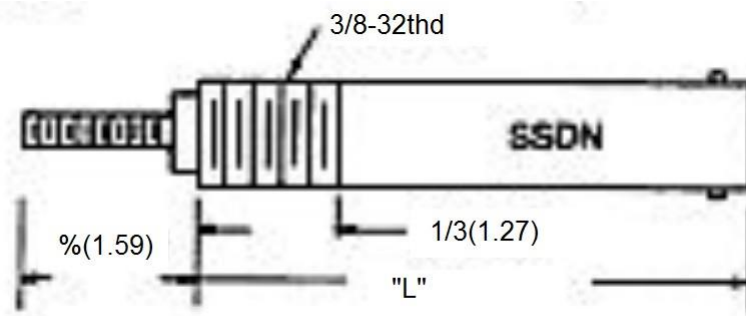


Figure 9: The current-viewing resistor model SSDN-10 from TandM Research [15].

Modified for legibility.

mylar layer allowing the threaded central conductor of the CVR to pass through the mylar and through the small hole on the hot-plate side where it was affixed by two brass nuts.

The SSDN-10 model was rated for an E_{max} of 2 Joules and had a risetime of 0.18 nanoseconds. Simulations run in circuit modeling program LT Spice and checked by hand showed that the power dissipated in the resistor would be well under the specified maximum as can be seen in Figure 10.

The entire setup was mounted on a table and hooked up to a common ground (see Figures 11 and 12).

3.6 Calibration Method

The voltage readings on the high voltage power supply were verified to within 0.1 volts by a multimeter before the experiment was run.

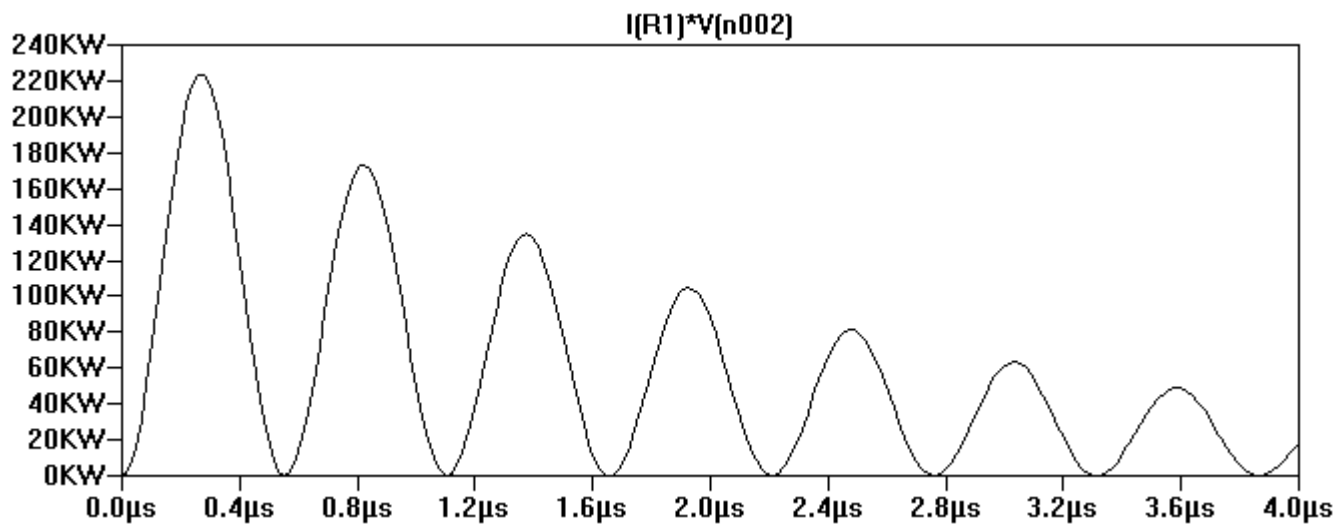


Figure 10: The anticipated power dissipated through the resistor as a function of time, as modeled in LTSpice. This shows the highest power case: a capacitor discharge of 2 kV which results in a total energy of 230 mJ compared to an E_{max} of 2 J.

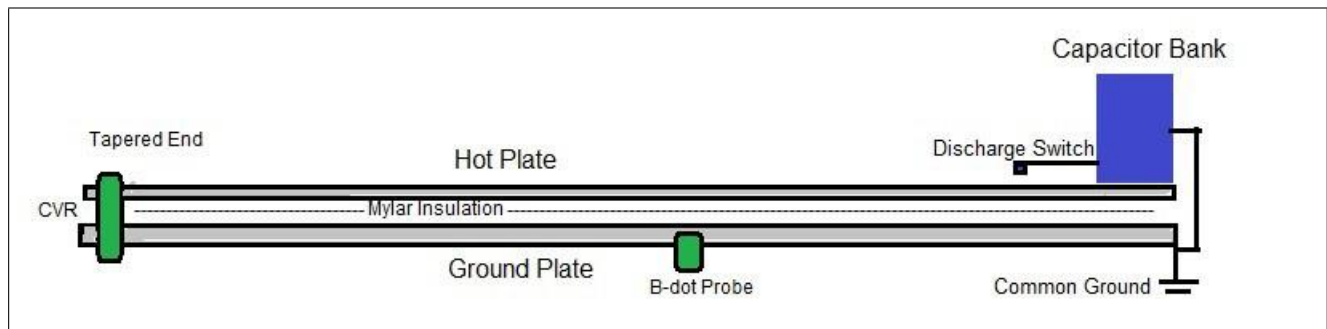


Figure 11: Diagram of the experimental setup. Side-view. Not to scale.



Figure 12: A photograph of the completed setup.

The CVR was attached to a 1 GHz scope by means of a 50-Ohm cable with two 5x attenuators. The attenuators were Tektronix BNC type (part number 011006003) with attenuation strength $14 \text{ dB} \pm 0.4 \text{ dB}$. The B-dot signal was a 50-Ohm cable terminated with a 50-ohm terminator to reduce reflection.

The capacitors were charged to 1 kV, 1.25, 1.5, and 2 kV and discharged into the plates. The voltage seen by the CVR and the B-dot were recorded and compared.

4 Results

Figures 13 through 16 are the results of the oscilloscope output for the measurements at each of the four voltages used. Five measurements at each voltage were taken for reproducibility although only one of each is shown.

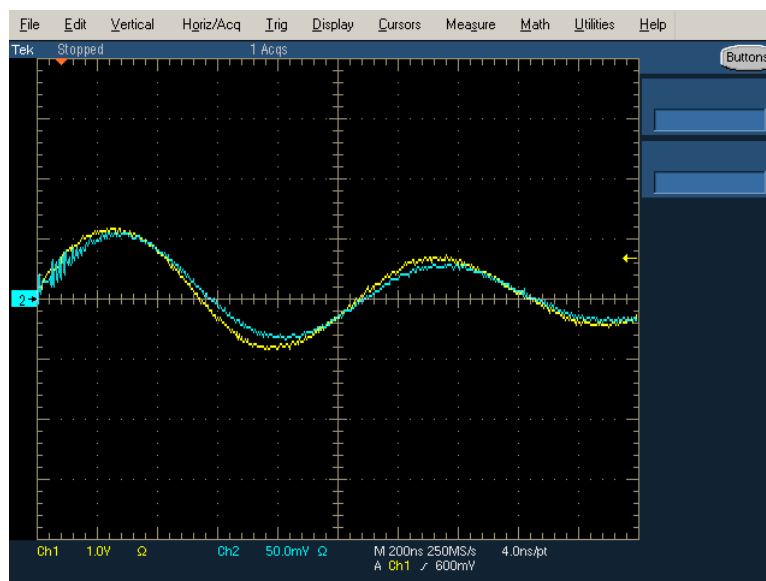


Figure 13: Capacitor discharge from 1 kV. Signal from the CVR is in channel 1 (yellow) and signal from the B-dot is in channel 2 (blue) of the oscilloscope which was triggered by the CVR signal.

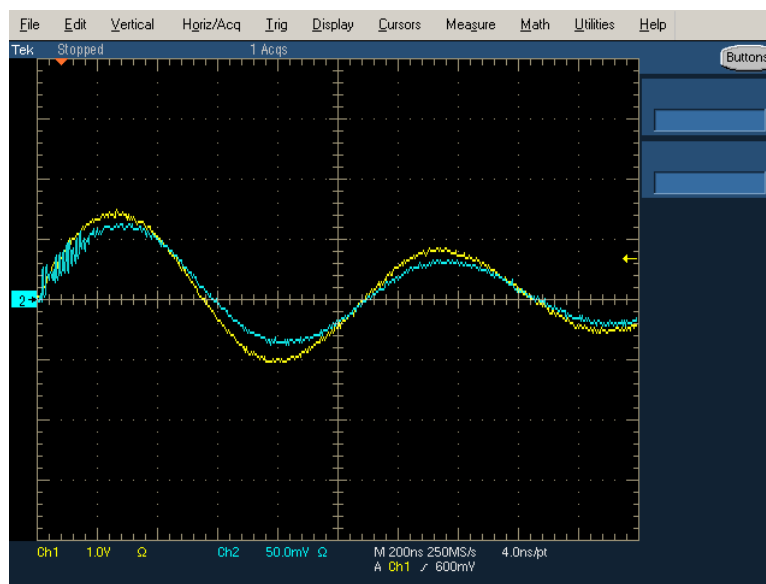


Figure 14: Capacitor discharge from initial charge of 1.25 kV. Signal from the CVR is in channel 1 (yellow) and signal from the B-dot is in channel 2 (blue) of the oscilloscope.

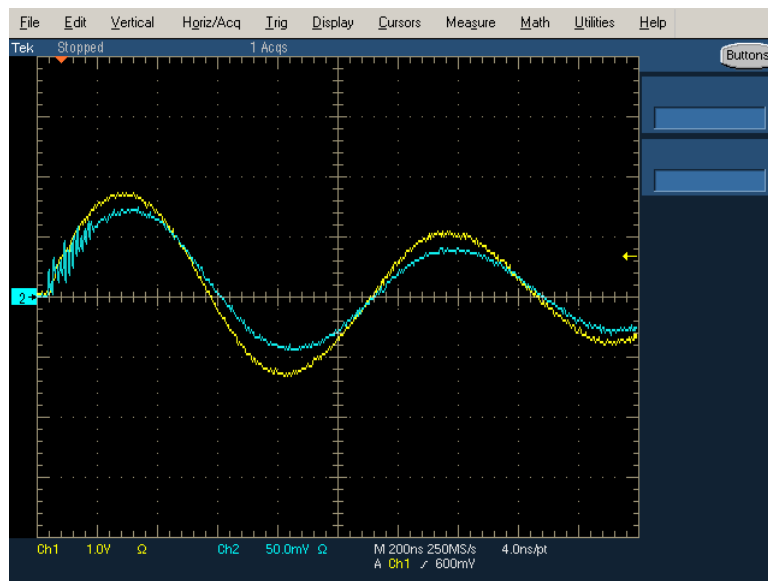


Figure 15: Capacitor discharge from 1.5 kV. Signal from the CVR is in channel 1 (yellow) and signal from the B-dot is in channel 2 (blue) of the oscilloscope.

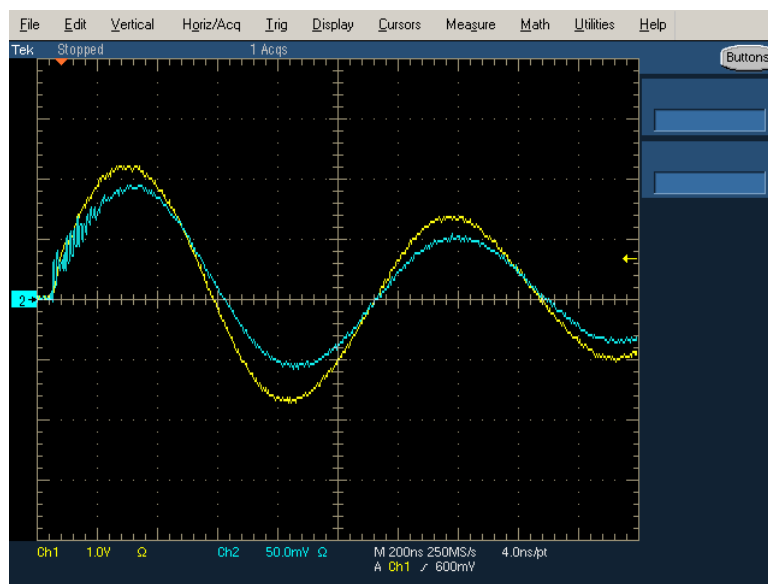


Figure 16: Capacitor discharge from a charge of 2 kV. Signal from the CVR is in channel 1 (yellow) and signal from the B-dot is in channel 2 (blue) of the oscilloscope.

5 Discussion and Analysis

To calibrate the B-dot probe signal, it was necessary to find the correspondance between it and the pre-calibrated CVR signal. Since the shape of the two signals matched, it was only necessary to apply a scaling factor to the B-dot signal to bring it to the same amplitude value as the reference CVR signal. This was done by taking the second positive peak of both signals and comparing them together to determine an appropriate factor to scale up the B-dot signal. The second peak was chosen as the one to perform the calibration on since it is the least noisy of the peaks. The first peak has a notably noisy rise in the B-dot signal due to transients in the system. Further discussion of the scaling factor is in Section 5.2.

5.1 Variance of the Runs

To gain an understanding of how the signal varied between runs, the results of five discharges at each of the four voltages were averaged together. This allows a mathematical look at how much variance there is between discharges at the same voltage and how repeatable is the calibration process. The variance of the shots from the mean is a statistical description of how much each run differs from the average.

The five runs were averaged together to produce a mean signal at the given voltage. Since only the second peak is used for calibration, the 3000 points in the

Table 1: Difference from the mean, V_{run}/V_{avg} , for each of the five CVR outputs at each voltage.

Difference from the mean				
Run Number	1 kV	1.25 kV	1.5 kV	2 kV
1	1.0203	0.9748	1.0261	0.9965
2	1.0147	1.0175	1.0078	0.9585
3	1.008	0.9627	0.9868	1.0199
4	0.9999	1.007	0.9932	1.0266
5	0.9571	1.038	0.9861	0.9985
Variance	0.0252	0.0309	0.017	0.0267

second peak for each run were divided by the 3000 points in the mean second peak to produce a voltage ratio, V_{run}/V_{avg} , representing the percent difference between each run and the mean. These results are summarized in Table 1 and Table 2.

Tables 1 and 2 show how much the signal changes between each discharge of the capacitors. We see that there is about 3% variation in the CVR signal between shots and 2-4% variation for the B-dot. This is a random uncertainty and any bias introduced in each measurement is small. The differences between the shots are likely due to inconsistencies in the switching technique used and random noise in the signal. Using automated switches to discharge the capacitor for each run

Table 2: Difference from the mean, V_{run}/V_{avg} , for each of the five B-dot outputs at each voltage.

Difference from the mean				
Run Number	1 kV	1.25 kV	1.5 kV	2 kV
1	1.0638	0.9970	1.0124	0.9983
2	0.9998	1.0383	0.9905	0.9720
3	0.9973	0.9635	1.0060	1.0095
4	0.9888	0.9928	0.9867	1.0222
5	0.9503	1.0084	1.0045	0.9979
Variance	0.0408	0.0271	0.0109	0.0185

would likely reduce the variance.

5.2 Scaling Factor

To find the scaling factor difference between the B-dot signal and the CVR signal, we focused on comparing the second peaks of the CVR and B-dot signal to each other. As mentioned previously, the second positive peak was chosen as it was the cleanest of the peaks.

It was found that the CVR signal preceded the B-dot signal in time by a fixed amount for each of the different voltages.

To resolve the delay offset between the two datasets, the channel number of the center of the peak was compared between the two. The channel number of the CVR data peak was used as the reference and an appropriate offset was applied to the B-dot data so that the two peaks occurred at the same x-value.

To reduce the noise of the data and aid in the process of curve fitting the raw data were averaged together in bins of 100 points where each point is in 0.4 ns bins. The binned data were then used to fit various functions for calibration.

5.3 Polynomial Fit

A fifth order polynomial was fitted to each data set using the entire second peak amplitude above the zero level (3000 points, 120 ns). The polynomial was gen-

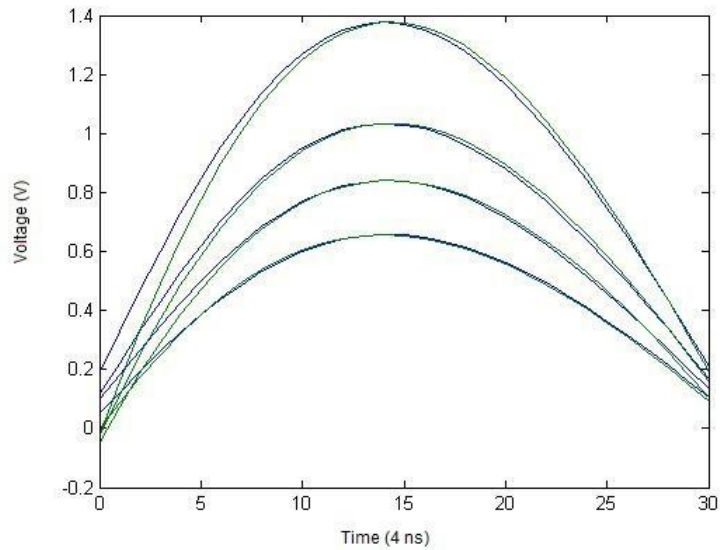


Figure 17: A 5-th order polynomial was fit to each data set in the vicinity of the second peak. The B-dot curve was scaled up to match the voltage of the CVR curve (see Section 5.4). The CVR curves are in blue and the B-dot curves are in green. Vertical axis shows voltage in units of volts and horizontal axis shows time in units of 4 ns.

erated by MATLAB's polyfit function. The results of this fit for each of the detectors at each voltage is shown in Figure 17.

The polyfit function uses the least-squares method of fitting a curve to the data. The squares of the differences (residuals) between the data and the curve were averaged together to analyze the goodness of the fit to the data. The results of this analysis are presented in Table 3.

The R^2 statistical test was used as another guarantor of the goodness of the

Table 3: The average residuals between the fit curve and the data.

Average Square Difference		
Voltage	CVR	B-Dot
1 kV	1.109E-4	7.14E-5
1.25 kV	1.837E-4	1.099E-4
1.5 kV	2.554E-6	1.626E-4
2 kV	4.554E-4	2.822E-4

polynomial curve f_i to the data. R^2 is defined as the sum of the squares of the residuals divided by the total sum of the squares.

$$R^2 = 1 - \frac{SS_{res}}{SS_{tot}} \quad (33)$$

$$SS_{res} = \sum_i (y_i - f_i)^2 \quad (34)$$

$$SS_{tot} = \sum_i (y_i - \bar{y})^2 \quad (35)$$

where y_i are the observed values and f_i are the values predicted by the curve. The R^2 values for each of the curves fit to the unbinned data are given in Table 4. The errors represent the variation between fits for different runs.

After binning the data (100 points per bin where each point is 0.4 ns wide) to average out the noise, the residuals were reduced, leading to a better fit. The average R^2 values for the binned data are given in Table 5.

Table 4: The R^2 goodness of fit values for the 5-th order polynomial curve fit to the unbinned data.

R^2 Values (Unbinned Data)		
Voltage	CVR	B-Dot
1 kV	0.9447 ± 0.0022	0.9495 ± 0.0024
1.25 kV	0.9672 ± 0.0013	0.9635 ± 0.0018
1.5 kV	0.9758 ± 0.0006	0.9750 ± 0.0009
2 kV	0.9864 ± 0.0002	0.9868 ± 0.0005

Table 5: The R^2 goodness of fit values for the 5-th order polynomial curve fit to the binned data. Each bin contained 100 points (40 ns).

R^2 Values (Binned Data)		
Voltage	CVR	B-Dot
1 kV	0.9889 ± 0.0024	0.9876 ± 0.0018
1.25 kV	0.9903 ± 0.0004	0.9881 ± 0.0009
1.5 kV	0.9912 ± 0.0005	0.9899 ± 0.0008
2 kV	0.9911 ± 0.0001	0.9902 ± 0.0004

5.4 Peak Matching

Once the polynomials f_i to the CVR signals at each voltage and the polynomials f_i to the corresponding B-dot signals were matched such that their peaks occurred at the same value, they were compared to determine if meaningful calibration could be done. In order to remove outliers caused by the signal being near 0, 250 points on each side of the curve were discarded from this analysis, leaving the 2500 points making up the peak of the signal. To find the error between the two polynomials at each capacitor voltage, each of the 2500 points on the polynomial curve was divided by the corresponding point on the scaled B-dot polynomial curve to determine the ratio between the two. The average ratio for each capacitor voltage is given in Table 6. A graphical representation of the difference between the two curves is given in Figure 18.

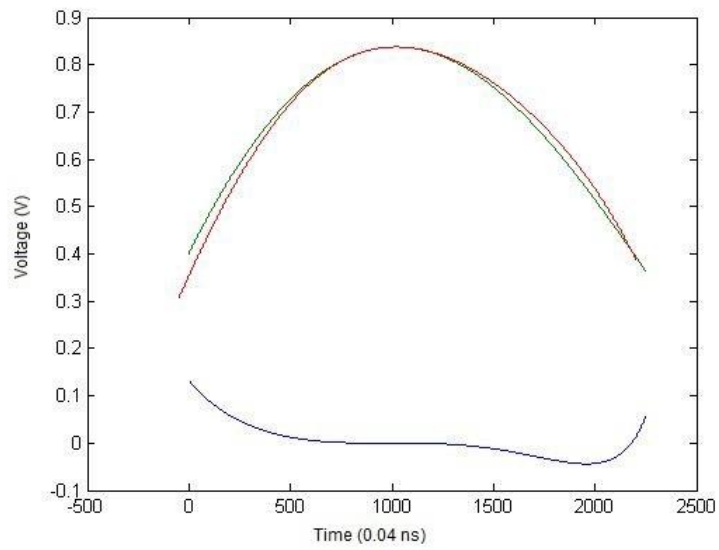


Figure 18: The polynomial curve matched to the B-dot is in red and the curve matched to the CVR is in green. Vertical axis is voltage and horizontal axis is channel number ($4E-11$ s). Below the curves is the ratio of the two curves minus 1 so that zero indicates that the two curves are equal at that point.

Table 6: Each of the 2500 points on the polynomial curve f_i to the CVR data were divided by the corresponding points on the scaled B-dot polynomial curve to measure how well the scaled signals matched.

Average Ratio (CVR/B-dot)	
Voltage	Average Ratio
1 kV	1.003 ± 0.004
1.25 kV	1.0042 ± 0.0014
1.5 kV	1.0002 ± 0.0013
2 kV	1.0121 ± 0.0005

6 Error Analysis

The factors by which the amplitude of the B-dot signal needed to be multiplied for the peaks to match are recorded in Table 7. The uncertainties in the scaling factor come from the variation in the runs and uncertainties in the fit of the polynomial used for scaling. These give an average error of 1.7%.

Table 7: The factors by which the B-dot signal needed to be multiplied to calibrate with the CVR.

Scaling Factors	
Voltage	Multiplication Factor
1 kV	21.2 ± 0.6
1.25 kV	22.6 ± 0.5
1.5 kV	23.5 ± 0.3
2 kV	23.7 ± 0.2
Average	22.8 ± 0.4

However, taking into account the 14 ± 0.4 dB attenuators applied to the CVR signal, the scaling factor is found to be 570 ± 30 for a total error of 5 %

The polynomial curves representing the B-dot and CVR match each other to an error of less than one percent on average and reduce the noise in the raw data. However, there is still enough variation in the runs for the error to exceed one

percent. Even if the signals were perfectly calibrated to each other, other limitations on verifying the true current signal include the error on the NIST calibration of the CVR (one percent) and the NIST calibration of the scope, which is also assumed to be on the order of one percent [16]. The attenuators used also have an intrinsic error of about three percent resulting in more than half of the error in the f_i calibration value. With better calibrated electronics, however, this setup could potentially provide calibration of under one percent error.

7 Future Work

This setup is a promising method for low-cost, customizable magnetic-field probe calibration. Some areas for further development include ways to reduce the error in the calibration and methods for generalizing the mounting of the probes to the strip-line so that probes of different geometries can be used.

7.1 Error Reduction

Using more precisely verified parts, especially the signal attenuators, could substantially reduce error in the calibration factor. It is believed by the author that the human factor in closing the switch to discharge the capacitors contributed in large part to the difference between shots at the same voltage. Automatic switching technology could be employed in the place of the human operator to achieve consistent discharges in the future. Fast, high-voltage switching could be used to provide consistency and shorter discharge times leading to better calibration. It is also noted that the curve fit improved at higher voltages. Running this experiment at even higher voltages than those used could potentially improve the signal-to-noise ratio and reduce the amount that each run varies from the others.

7.2 Interfacing With Other Probes

In this work, only one type of B-dot probe was used. The probe was fixed by screws into the ground plate. Although the current setup allows easy removal and mounting of B-dot probes of the same type as the one used in this work, the system could be designed to allow other models of B-dot probes to be mounted and calibrated. It was conjectured that an interface could be designed that would allow a larger B-dot probe to mount onto the ground plate. This would have the advantage of not needing to remachine the plates each time a new probe needed to be tested; one could simply mount a different adapter.

8 Conclusion

We developed a simple method for calibrating B-dot magnetic field probes for use in high-current experiments, particularly involving pulsed-power. The calibration system was shown to generate uniform current through the use of electrophysics modeling software. This uniform current was used to provide the calibration current to a B-dot magnetic field probe. The signal produced by the probe was compared to a pre-calibrated current-viewing resistor which had a resistance known to within one-percent precision. Due to uncertainties in the electronics used and random error introduced in the system, the calibration of the B-dot obtained an uncertainty of 5 %. The field calibration value was that the B-dot signal needed to be scaled up by a factor of 570 ± 30 .

References

- [1] E. T. Everson, P. Pribyl, C. G. Constantin, A. Zylstra, D. Schaeff N. L. Kugland, and C. Niemann Design, construction, and calibration of a three-axis, high-frequency magnetic probe as a diagnostic for exploding plasmas. *Rev. Sci. Instrum.* 80, 113505 (2009).

- [2] Anne van Arsdall, Pulsed Power at Sandia National Laboratories: The First Forty Years.

- [3] Sanford, Thomas W.L. Overview of the Dynamic-Hohlraum X-ray Source at Sandia National Laboratories.

- [4] Hutchinson, I.H. Electromagnetic Interactions. 1999. Web. 28 Oct. 2014. <<http://ocw.mit.edu/courses/nuclear-engineering/22-105-electromagnetic-interactions-fall-2005/readings/>>.

- [5] S. Humphries, Jr. Principles of Charged Particle Acceleration. 1997.

- [6] Hanson, Barry. "Damped Oscillators." Inductors. 10 Nov. 2012. Web. 28 Oct. 2014. <<http://www.coilgun.info/theoryinductors/dampedoscillator.htm>>.

- [7] Appelgren, Patrik Gigawatt Pulsed Power Technologies and Applications. Doctoral Thesis, School of Electrical Engineering Space and Plasma Physics, Royal Institute of Technology, Stockholm, Sweden.

- [8] M. P. Reilly, W. Lewis, and G. H. Miley, Magnetic field probes for use in radio frequency plasma. *Rev. Sci. Instrum.* 80, 053508 (2009).
- [9] S. Messer, D.D. Blackwell, W. E. Amatucci, and D. N. Walker, Broadband calibration of radio-frequency magnetic induction probes. *Rev. Sci. Instrum.*, 77.115104 (2006).
- [10] R. Spielman (personal communication), Jan 9, 2014.
- [11] L.A. Morton, E. T. Everson, C. G. Constantin, D. Schaeff, P. Pribyl, and C. Niemann, Calibration of a Magnetic Field Probe as a Diagnostic for Laser-Produced Plasma 2010.
- [12] Engelhardt, Mike. *LTspice IV*. (Version 4.21i) [Software] Linear Technology. Available from <http://www.linear.com/designtools/software/>. 2014.
- [13] REMCOM. *XFtd7* 7. (Version 7.3.2) [Software] REMCOM. Available from <http://www.remcom.com/xf7>. 2014.
- [14] REMCOM XF7 User Guide
- [15] TandM Research website. <www.tandmresearch.com>.
- [16] Guidelines for Evaluating and Expressing the Uncertainty of NIST Measurement Results. 1994.